Soft Matter

Fabric-based jamming phase diagram for frictional granular materials

Journal:	*Soft Matter*
Manuscript ID	SM-ART-09-2023-001277.R2
Article Type:	Paper
Date Submitted by the Author:	11-Mar-2024
Complete List of Authors:	Wen, Yuxuan; University of Colorado Boulder, Civil, Environmental and Architectural Engineering Zhang, Yida; University of Colorado Boulder, Civil, Environmental and Architectural Engineering

Fabric-based jamming phase diagram for frictional granular materials

Yuxuan Wen[1], Yida Zhang[2*]

Abstract

Jamming phase diagram maps the phase states of granular materials to its intensive properties such as shear stress and density (or packing fraction). We investigate how different phases in jamming phase diagram of granular materials are related to its fabric structure via three-dimensional discrete element method simulations. Constant-volume quasi-static simple shear tests ensuring uniform shear strain field are conducted on bi-disperse spherical frictional particles. Specimens with different initial solid fractions are sheared until reaching steady state at a large shear strain (200%). The jamming threshold in terms of stress, non-rattler fraction, and coordination numbers (Z's) of different contact networks are discussed. The evolution of fabric anisotropy (F) of each contact network during shearing is also examined. By plotting the fabric data in the F-Z space, a unique critical fabric surface (CFS) becomes apparent across all specimens, irrespective of their initial phase states. Through the correlation of this CFS with fabric signals corresponding to jamming transitions, we introduce a novel jamming phase diagram in the fabric F-Z space, offering a convenient approach to distinguish the various phases of granular materials solely through the direct observation of geometrical arrangements of particles. This jamming phase diagram underscores the importance of the microstructure underlying the conventional jamming phenomenon and introduces a novel standpoint for interpreting the phase transitions of granular materials that have been exposed to processes such as compaction, shearing, and other complex loading histories.

[1] Ph.D. Candidate, Dept. of Civil, Environ. and Architect. Eng., University of Colorado Boulder, Boulder, CO, USA.

[2] Assistant Professor, Dept. of Civil, Environ. and Architect. Eng., University of Colorado Boulder, Boulder, CO, USA.

* Corresponding author. Email: yida.zhang@colorado.edu

1 Introduction

Jamming is a phenomenon where amorphous disordered materials such as granular soils, colloidal suspensions, emulsions, and glasses transform from a fluid-like to a solid-like state and has been widely observed in nature and engineering practice. This abrupt transition is often described by a surface in the 3-dimentional (3D) space of temperature, load, and the inverse of density.[1] For granular materials which are athermal (i.e., the thermal fluctuation is insufficient to alter their packing configurations), the corresponding jamming phase diagram (JPD) becomes a 2-dimentional (2D) plane of shear stress τ vs. packing fraction ϕ.[2, 3] O'Hern and coworkers[4, 5] investigated the onset of jamming for frictionless granular packings by increasing density at zero shear stress and found that the jamming point J has a packing fraction ϕ almost identical to that of the random close packing, i.e., $\phi_J \approx \phi_{RCP} \approx 0.84$ in 2D, and $\phi_J \approx \phi_{RCP} \approx 0.64$ in 3D cases.

Frictional granular systems, however, could jam over a finite range of ϕ with ϕ_J being dependent on the sample preparation protocols and system parameters. For example, ϕ_J decreases when particle-particle friction coefficient μ increases or compression rate decreases.[6-8] The random close packing ϕ_{RCP} is approximately the upper bound of ϕ_J for frictional granular systems.[9] Song and coworkets[10] analytically derived the minimum ϕ of 3D random loose packings $\phi_{RLP}^{\min} \approx 0.536$ and predicted it to be the theoretical lowest threshold of ϕ_J for isostatic jammed frictional granular materials if μ is infinitely large. This is supported by the observation that $\phi_{RLP}^{\min} \approx 0.536$ is close to the lowest stable ϕ ever reported for monodisperse spheres.[11] Therefore, a frictional granular packing with $\phi_{RLP}^{\min} < \phi < \phi_{RCP}$ can be either jammed or unjammed depending on its preparation protocol,[12] blurring the phase transition boundary depicted in classical JPDs.

Bi and coworkers[9] conducted 2D pure shear tests on photoelastic disks isotropically compressed to initially unjammed states $\phi < \phi_J$. In their experiments, ϕ_J is closer to the upper

bound ϕ_{RCP} as their sample preparation involves gentle tapping which can break force chains, release the friction buildups at contacts, and thus relax the system's stress to the lower values. When shearing is followed, the specimen may stay unjammed, exhibit weak resistance to shear, or develop strong shear stress depending on the initial ϕ. They have thus proposed two more intermediate phases for frictional packings, namely the "fragile" and the "shear jammed" phases, in addition to the unjammed and jammed phases depicted by the classical JPD for frictionless systems. The fragile state is able to support loads only along the compatible direction (i.e., the direction that strong force network percolates) without undergoing plastic rearrangement.[13] The shear jammed phase can resist perturbance in all directions and thus is a truly jammed state induced by shear. Recently, Zhao and coworkers[14] further enriched the generalized JPD[9] by locating the boundaries between the unjammed, the shear jammed, and the fragile states on the mean stress p vs. packing fraction ϕ plane via a series of multiring Couette shear experiments on photoelastic disks.

While JPD offers a unifying framework to discuss the phase transition of granular materials in terms of macroscopic variables (p, τ, ϕ), the underlying micro-mechanisms that governs such transition can be only studied by tracking the microstructural evolution of the granular assembly. Existing studies on JPD have extensively focused on the isotropic measures of granular microstructure such as the coordination number Z,[5, 10] the non-ratter fraction f_{nr},[9] and the contact-force statistics.[15-17] It has been found that frictional granular materials will develop strong fabric anisotropy when subjected to shearing.[18-20] A series of true triaxial Discrete Element Method (DEM) simulations shows that steady-state granular flow is always anisotropic, the degree of which depends on the confining pressure and shear mode.[21] Recent DEM simulations investigating the flow-arrest transition[22, 23] that is similar to the shear-jamming have also revealed that fabric anisotropy is a crucial variable influencing the transition between solid-like and fluid-like state. X-ray microtomography (X-μCT) observations of sheared sand specimens indicate that the macroscopic stress-strain behavior is tightly related to the evolution of fabric anisotropy.[24, 25] An important modification of the classical critical state theory[26] is hence proposed to consider fabric anisotropy[27] for modeling

the quasi-static stress-strain response of granular soils.[28-30] The characteristics of fabric anisotropy and its relationship with granular jamming have been explored in several previous studies.[9, 14, 31] However, they fall short of considering fabric anisotropy as an essential variable in a JPD for distinguishing various phases including jammed, shear jammed, fragile, and others. This might be due to the intuition that a granular assembly develops trivial anisotropic microstructure at low mean stress levels, and a single scalar indicator such as Z would suffice for phase characterizations.

Our recent DEM experiments[32, 33] have challenged this picture. Specifically, as shown in Fig. 1, we found unjammed (or "liquefied" in soil mechanics terminology) frictional granular specimens exhibits clear fabric anisotropy F with $p \approx 0$ maintained throughout under zero gravity condition. The F value of unjammed specimens is strongly correlated with the Z for the full range of $0 < Z < Z_{jam}$. This line smoothly joins the critical-state fabric data of jammed specimens ($Z > Z_{jam}$) and forms a unique *critical fabric surface* (CFS) in the F-Z plane (Fig. 1a). Similar results have also been identified[34] where the pressure-controlled simulations lead to a CFS in the jammed region and a model is proposed for describing it. The CFS in Fig. 1a can also be visualized in the principal space of the fabric tensor (Fig. 1b) substantiated by data from true triaxial shear tests at different principal stress and strain ratios. Therefore, the CFS can be thought of as a universal attractor for all fabric states upon shearing, regardless of the shear mode and whether the sample is initially jammed or not. Moreover, on the fabric F-Z plane, one can reasonably distinguish the fabric paths and the portion of the CFS that belongs to samples that develop a finite shear stress at steady-state (jammed) and those do not (unjammed). This preliminary observation suggests that there may exists a one-to-one mapping between the conventional JPD in the τ-ϕ[5, 35-38] (or p-ϕ[9, 14]) plane and that in the fabric F-Z plane.

Motivated by the above, the objective of this paper is to: 1) systematically investigate the fabric characteristics of frictional granular materials near jamming transition; 2) develop a jamming phase diagram with fabric variables for the determination of phase state. Toward this goal, 3D DEM simulations of constant volume simple shear on bi-disperse frictional

spheres are conducted (Section 2). The stress-strain response and the jamming thresholds as well as the conventional JPD are discussed in Section 3. In Section 4, the fabric characteristics including Z and F for the non-rattler, total, and strong contact networks are explored and interpreted with reference to CFS, which leads to the development of a jamming phase diagram in F-Z space. Section 5 discuss the relationship between the fabric tensor and non-rattler fraction and Section 6 summarizes the main conclusions and discusses possible future extensions of this work.

2 Methodology

2.1 Sample preparation

The open-source DEM code YADE[39] is adopted to conduct constant volume simple shear numerical tests. In designing the simulation protocol, we have largely referred to the recent multiring Couette shear setup[14] and formulated the following objectives: 1) be able to reproduce initially unjammed specimens with $\phi < \phi_J \approx \phi_{RCP}$; 2) preserve the uniform shear strain field across the specimen; 3) enforce the quasi-static condition; and 4) be able to shear to infinite shear strain. With these goals in mind, the details of the DEM simulation are reported below.

Each test consists of two stages namely sample preparation and simple shear. In the preparation stage, N spheres are generated sparsely without any contact enclosed in a rectangular prism with four periodic lateral boundaries and two rigid walls on the top and the bottom. To avoid crystallization,[40] binary mixture with particle diameter ratio $d_1 : d_2 = 1.4 : 1$ and particle number ratio $N_1 : N_2 = 1 : 1$ is adopted.[4, 8, 41] A compression procedure similar to Zhang and Maske[7] is then applied, during which periodic boundaries and rigid walls moves inward with a constant rate (volumetric strain rate $\dot{\varepsilon}_v = 0.05\ \mathrm{s}^{-1}$) and stops when the specified ϕ is reached, followed by a relaxation step until p becomes stable (i.e., equilibrium). The total number of particles N is calculated such that the specimen reaches the specified ϕ with a dimension of $16d_1 \times 16d_1 \times 12d_1$ [37, 42] at the end of compression. Note that the spheres are set as

frictionless (μ = 0) during the compression to mimic the tapping process adopted in the preparation of photoelastic specimens,[9, 14] where friction buildups are effectively removed and the specimen is able to stay unjammed up to $\sim\phi_{RCP}$. Using this protocol, we have prepared a series of specimens with ϕ ranging from 0.45 to 0.64 at an increment of 0.01. After the specified ϕ is reached at the end of compression, μ is updated from 0 to 0.5, a typical value for frictional granular materials like sand.[43] This μ-adjusting technique is also commonly used in the granular mechanics community for obtaining specimens with different initial densities under the same confining pressure.[44-46]

2.2 Shearing algorithm

Before shearing, we agglomerated the particles located at the very bottom ($0 < z < 1.5d_1$) and top ($10.5d_1 < z < 12d_1$) of the specimen to form particle walls, as shown in Fig. 2(a). Shearing is performed through an athermal quasi-static (AQS) procedure[47, 48]: first, a shear strain increment $\Delta\gamma$ is affinely imposed on each particle and the particle walls (Fig. 2(a)). This is followed by a relaxation stage where the system runs an additional N_t timesteps with shearing paused to allow dissipation of the kinetic energy (E_k) and return to equilibrium. The reason for adopting particle walls is to avoid slippage at the shear boundaries when the assembly is being relaxed. In addition, it reduces the overall complexity of contact type such that the contact within the whole granular system is consistent (i.e., particle-particle contact). It is important to distinguish our shear procedure from the conventional wall-driven mechanism, where shearing is induced solely by driving the walls, often resulting in non-uniform velocity field and strain localization in the specimen.[49-51]

We have surveyed a range of N_t values and found that N_t = 10 can ensure the maximum E_k of the whole granular system in all simulations at the end of relaxation is sufficiently smaller than a kinetic energy threshold while offering a manageable simulation time to achieve γ = 200%. This kinetic energy threshold is set to be $3\times10^{-4}m_1gd_1$ where m_1 equals to the mass of a sphere with diameter d_1 and g = 9.81m/s^2. The equivalent shear strain rate can be calculated by $\dot{\gamma} = \Delta\gamma / (N_t\Delta t)$ and is set to 0.5% s^{-1} (i.e., $\Delta\gamma = 0.05\Delta t$ with Δt the value of a

single timestep) in all the simulations presented hereafter. Gravity is not activated in our simulation to maintain close analogy with the 2D multiring Couette experiments[14] where all disks are placed horizontally.

The granular assembly sandwiched by the particle walls is the actual representative volume element (RVE) where the stress, strain, and fabric data are extracted. The effective height h of the sample is determined using the following procedure: the macroscopic shear stress can be calculated by summing all contact forces in the y direction on the top particle-wall divided by the cross-section area $\tau = \sum f_y \big/ A$ where $A = 16d_1 \times 16d_1$. The average Cauchy stress can be also calculated according to the Love-Weber formula:[52]

$$\sigma_{ij} = \frac{1}{V} \sum_{c \in C} f_i^{(c)} l_j^{(c)} \tag{1}$$

where the sum is over all contacts C; f the contact force; l the branch vector joining centers of the two particles at contact c; V the volume of the specimen. For our simulations, the calculation of σ_{ij} in Eq. (1) should exclude the clumped particles in the C set and use the true specimen height h in calculating the specimen's volume $V=A \times h$. The applied τ is compared with the corresponding stress component σ_{zy}, and it is determined that $h = 9d_1 + 0.5d_2$ to have $\tau = \sigma_{zy}$ (Fig. 2(b)).

Note that Zhao and coworkers[14] have reversed the shear direction after reaching the designated γ level to probe the stability of the developed force chain network, which was used to distinguish the fragile (F) and the shear jammed (SJ) states. Our study, however, is constrained by the available computational capability and the long simulation time of 3D assemblies. To avoid compromising the thoroughness of this simulation campaign (i.e., reducing the total number of tests or shortening the maximum shear strain), we have opted to reserve the shear reversal tests for future studies, and focus the present analyses on the fabric signals of apparent jamming induced by monotonic shear without distinguishing the F and SJ states.

2.3 Contact model and parameters

The Hertz-Mindlin contact law[53] is adopted for our simulations. The normal force and tangential force with the consideration of Coulomb friction of a contact between particles 1 and 2 are:

$$F_n = \underbrace{\frac{4}{3} E_{eff} \sqrt{R_{eff} \delta_n} \delta_n}_{F_n^{elastic}} + \underbrace{2\sqrt{\frac{5}{6}} \frac{\ln c_r}{\sqrt{\ln^2 c_r + \pi^2}} \sqrt{2 m_{eff} E_{eff} \sqrt{R_{eff} \delta_n}} v_n}_{F_n^{viscous}} \quad (2)$$

$$F_t = \min\left(\underbrace{8 G_{eff} \sqrt{R_{eff} \delta_t} \delta_t}_{F_t^{elastic}} + \underbrace{2\sqrt{\frac{5}{6}} \frac{\ln c_r}{\sqrt{\ln^2 c_r + \pi^2}} \sqrt{8 m_{eff} G_{eff} \sqrt{R_{eff} \delta_n}} v_t}_{F_t^{viscous}} , \mu F_n \right) \quad (3)$$

where E is the Young's modulus; G is the shear modulus; R is the particle's radius; m is the particle's mass; c_r is the coefficient of restitution in the range of 0 to 1; μ is the Coulomb friction coefficient; δ_n, v_n and δ_t, v_t are the overlap distances and the relative velocities between the two contacting particles along the normal and tangential directions, respectively; subscript '*eff*' represents effective variables, where $m_{eff} = \left(\frac{1}{m_1} + \frac{1}{m_2} \right)^{-1}$, $R_{eff} = \left(\frac{1}{R_1} + \frac{1}{R_2} \right)^{-1}$, $G_{eff} = \left(\frac{2-\nu_1}{G_1} + \frac{2-\nu_2}{G_2} \right)^{-1}$ and $E_{eff} = \left(\frac{1-\nu_1^2}{E_1} + \frac{1-\nu_2^2}{E_2} \right)^{-1}$ with ν being the Poisson's ratio; $F_n^{elastic}$ and $F_n^{viscous}$ represents the elastic and viscous term of the normal contact force respectively; $F_t^{elastic}$ and $F_t^{viscous}$ represents the elastic and viscous term of the tangential contact force respectively. The critical time step $\Delta t_{cr} = \min\left(R_i \sqrt{(\rho_g)_i / E_i} \right)$ is an important factor that influences the simulation stability and speed, where subscript 'i' represents the i^{th} particle[39]. A safety factor 0.3 is further adopted such that $\Delta t = 0.3 \Delta t_{cr}$ to ensure the stability of simulation. Table 1 lists the parameters used in the DEM simulations of this study. A relatively small value of E is adopted here to be able to use a relatively large time step.[21, 54] Our initial simulations have adopted the viscous term in this contact model. The computational time required to dissipate kinetic energy during the relaxation, however, was found to be excessively long. As a result, we adopted Cundall's numerical damping[55], shown in Eq. (4) and has already been implemented in YADE[39, 56], instead of the viscous damping

(i.e., setting $F_n^{viscous} = F_t^{viscous} = 0$) to accelerate the computation.

$$\Delta\mathbf{F} = -\beta \, \mathrm{sign}\left(\mathbf{F}\cdot\mathbf{v}\right)\mathbf{F} \tag{4}$$

where **F** = total force vector on a particle, **v** = particle's velocity vector, β = Cundall's damping coefficient, $\Delta\mathbf{F}$ = damping force on a particle. The Cundall's numerical damping is implemented by introducing an additional force that is directly proportional to the total force exerted on a particle. This force aligns with the total force when the angle between the total force and the particle's velocity exceeds 90 degrees, and opposes the total force when the angle is smaller than 90 degrees. [39]

Table 1. Parameters in DEM simulations

Parameters	Value
Grain density ρ_g	2650 kg/m^3
Particle diameter d_1	1.4 cm
Young's modulus E	200 MPa
Poisson's ratio v	0.2
Friction coefficient μ	0.5
Cundall's damping β	0.2

2.4 Fabric tensor definition

The fabric structure of a granular packing can be quantified by the statistics of particle orientation,[57] void vector,[58] or contact normals.[59] For the spherical particles investigated in this study, we focus the fabric characterizations based on the contact network statistics. Consider the following directional distribution function of contact normals:[59]

$$\rho(\mathbf{n}) = \frac{2N_c}{N}\bar{\rho}(\mathbf{n}) \tag{5}$$

where **n** is the unit contact normal vector; $\bar{\rho}(\mathbf{n})$ is the directional distribution density of contact normals; N and N_c are the total number of particles and contacts, respectively. The integration of $\rho(\mathbf{n})$ over all direction immediately gives the coordination number, Z:

$$\int \rho(\mathbf{n})\, d\Omega = \int\int \rho(\theta,\varphi)\sin\theta d\theta d\varphi = \frac{2N_c}{N} = Z \tag{6}$$

where Ω is the solid angle; θ is the polar angle; φ is the azimuth. The fabric tensor of the first

kind can be defined as:[59]

$$G_{ij} = \int \rho(\mathbf{n}) n_i n_j d\Omega = \int\int \rho(\theta,\varphi) n_i n_j \sin\theta d\theta d\varphi \tag{7}$$

where the trace of G_{ij} is exactly Z (i.e., $Z = G_{kk}$). In practice, G_{ij} can be calculated from the discrete data of contact normals by:

$$G_{ij} = \frac{2}{N}\sum_{k=1}^{N_c} n_i^{(k)} n_j^{(k)} \tag{8}$$

Alternatively, one can also approximate $\rho(\mathbf{n})$ by a second-order fabric tensor E_{ij}:[59]

$$\rho(\mathbf{n}) \approx \frac{1}{4\pi} E_{ij} n_i n_j \tag{9}$$

One can show that the mean spherical part of E_{ij} is Z (i.e., $Z = E_{kk} / 3$) by integrating Eq. (9) over the whole spherical surface (i.e., $\theta\in[0,\pi]$ and $\varphi\in[0,2\pi]$). It is also possible to express E_{ij} in terms of G_{ij} by multiplying Eq. (9) with $n_k n_l$ and integrating over the whole spherical surface,

$$E_{ij} = \frac{15}{2}\left(G_{ij} - \frac{1}{5} G_{kk}\delta_{ij} \right) \tag{10}$$

The deviatoric part of E_{ij} follows:

$$F_{ij} = E_{ij} - \frac{1}{3} E_{kk}\delta_{ij} \tag{11}$$

Substituting Eq. (11) into Eq. (9) gives:

$$\rho(\mathbf{n}) \approx \frac{1}{4\pi}\left(Z + F_{ij} n_i n_j \right) \tag{12}$$

which can be viewed as the spherical harmonic expansion of $\rho(\mathbf{n})$ truncated to the second order[59]. In all of our simulations, the mean fabric will be monitored by tracking the coordination number ($Z = E_{kk}/3$) and the fabric anisotropy will be characterized by the second invariant of F_{ij}, i.e., $F = \sqrt{(3/2) F_{ij} F_{ij}}$. The normalized fabric anisotropy is defined as the ratio between fabric anisotropy and the coordination number: $\bar{F} = F / Z$.

Note that the contact-based fabric measures strongly depend on how one defines the contact network. Past studies on granular jamming usually exclude "rattlers" which are particles that do not participate in the load-bearing network and only inspect the contact

statistics of non-rattler particles. While the physical definition of rattler is unique (i.e., relying on constraint counting or inspecting if the central particle can move freely with neighboring particles fixed), the practical implementations for identifying rattlers vary across different studies. This variation includes considering particles with contact numbers less than one,[41, 60, 61] two,[9, 14, 62, 63] three,[64] and four,[65] reflecting different criteria adopted for the purpose of simplicity. Here we adopt the implementation with the contact number less than 2 to be consistent with that in simple/pure shear tests of photoelastic disks,[9, 14] in calculating the fabrics of the non-rattler contact network. An iterative method that was recently developed[66] and closely aligned with the method originally proposed for jamming in hard sphere packings[67], offers a notably more rigorous approach to identifying ratter and may be adopted in future studies. Alternatively, fabric tensor defined based on the total contact network can be useful for granular system at very loose packings near the granular gas state. In such condition, most particles become rattler, and Eq. (5) becomes ill-defined for the non-rattler contact network but is still valid for the total contact network. Finally, the total contact network can be decomposed into two subnetworks of strong contacts and weak contacts.[19] The strong contacts carry a net force f larger than the average contact force of the whole network $\langle f \rangle$ while $f < \langle f \rangle$ for weak contact network. In this study, fabric tensors of the non-rattler, the total, and the strong contact networks are all investigated, and they are marked with subscripts "*nr*", "*t*", and "*s*", respectively. Note that the value of N is set as the number of non-ratter particles (N_{nr}) in calculating the non-rattler fabric tensor in Eq. (5),[9, 14] while N is the number of all particles for calculating the total- and the strong- contact fabric tensors.[32, 33]

3 Jamming thresholds

3.1 Stress space

When investigating the jamming phenomena, a crucial step is to ascertain the jamming thresholds, which can be defined in relation to ϕ, p, and f_{nr}, etc. Fig. 3(a) presents the mean stress $p = \sigma_{kk}/3$ of all specimens during steady state (also known as the "critical state")

277 shearing. Notably, the relationship between critical state mean stress (p_c) and ϕ exhibits an
278 opposite trend clearly distinguished at $\phi = 0.57$, and the error bar in $\phi < 0.57$ is higher than
279 that in $\phi > 0.57$. When $\phi \geq 0.57$, p_c diminishes with ϕ in a power-law relationship as ϕ
280 decreases, which can be described as:[7]

281 $$\frac{p_c}{p_a} = a_1 \left(\phi - \phi_c\right)^{b_1} \tag{13}$$

282 where p_a is the atmosphere pressure (101.3kPa), a_1, b_1 and ϕ_c are the fitting parameters. The
283 best-fit results, yielding the highest R^2 value of 0.9943, indicate $a_1 = 154.6031$, $b_1 = 1.1770$,
284 and $\phi_c = 0.5700$, are shown in the subplot of Fig. 3(a). Note that these parameters are system
285 and protocol dependent.[12] The calibrated ϕ_c serves as the threshold to distinguish between
286 shear jammed (including fragile) and unjammed specimens within our system. For
287 consistency with the Couette shear experiment we are simulating,[14] this threshold will be
288 denoted as ϕ_F. At $\phi_F = 0.57$, $p_c = 3$kPa, hence, a noise threshold $p_{noise} = 3$ kPa is identified and
289 adopted as a criterion to determine whether a packing is shear jammed (including fragile)
290 during monotonic shearing.[14] The implementation of p_{noise} represents a simplified approach to
291 determine jamming. It is important to note that the transition between jamming and
292 unjamming is notably intermittent and stochastic, characterized by pronounced finite size
293 effect.[22, 68] The shear strain needed for p to reach p_{noise} (jamming) exhibits increasing
294 divergence as ϕ decreases and deviates from ϕ_J. When subjected to a larger shear strain, p
295 may attain the specified p_{noise} for specimen with a smaller ϕ, indicating a shift in the onset of
296 shear jamming. This implies the assigned value of p_{noise} might vary with changes in system
297 size. Understanding these statistical uncertainties is pivotal for precisely defining the
298 boundary between jammed and unjammed states, and these aspects need to be thoroughly
299 investigated in future studies.

300 Fig. 3(b) displays the so-called "critical state line" (CSL) on e-p plane, where e is the void
301 ratio defined as the void volume over the solid volume and is related to ϕ by $e = (1-\phi)/\phi$. In
302 critical state soil mechanics,[69] only the data in the jammed region is considered, and the
303 expression of CSL is:

$$e_c = e_\Gamma - \lambda\left(\frac{p}{p_a}\right)^{\xi} \tag{14}$$

where e_Γ, λ and ξ are the fitting parameters. Their values are 0.7597, 0.0540 and 0.6644 respectively for the current system. Following the compression protocol in Section 2, the isotropic jamming point is detected at $\phi_J = 0.638 \approx \phi_{RCP}$ with an initial p slightly exceeds p_{noise}. We noted that it is impossible to generate an isotropic specimen passing this point ($\phi > \phi_J$ or $e < e_J$) without maintaining a finite pressure ($> p_{noise}$) on the boundary. Thus, on the same e-p plane, there should be a densest state line (DSL) that no specimen's (e, p) data can exist below it. This conceptual line is sketched in Fig. 3(b). The DSL should be monotonically decreasing, as the achievable densest state should have smaller void ratio e at higher mean stress levels p due to elastic deformation of the grains and contacts. The (e, p) state of the packing should always evolve above this DSL, influenced by particle attributes such as stiffness and morphology (including shape and grain size distribution). A state falling below the existing DSL should require changes in the geometrical characteristics of the particles through processes like grain crushing and asperity breakage, etc. The concept of DSL aligns closely with the notion of minimum void ratio e_{min} which is an impact index for defining granular soils' relative density and compactness in geotechnical engineering. [70-72] The precise determination of DSL and its correlation with particle stiffness and morphology exceeds the scope of this paper.

Fig. 3(c) and (d) presents stress-strain evolution and stress paths in τ-ϕ and q-p plane of shear jammed specimens with $\phi \geq \phi_F$. It shows that stress becomes stable around $\gamma = 1.6$~2.0. Consequently, the properties of the specimens at the steady/critical state are determined by averaging their values within this γ range, thereby mitigating the influence of data oscillation in DEM simulations. Fig. 3(d) demonstrates that all shear jammed specimens converge to the same critical state stress ratio $\eta_c = 0.61$.

3.2 Non-rattler fraction

Non-ratter fraction f_{nr} is defined as the ratio between the number of non-rattler particles (N_{nr}) and the number of total particles (N). Fig. 4(a) presents the evolution of f_{nr} during

shearing. It is observed that: 1) the specimen with ϕ = 0.64 is initially jammed and has a f_{nr} larger than a reference value 0.855 prior to shearing; 2) For initially unjammed specimens with ϕ = 0.45~0.63, f_{nr} increases as the shear strain accumulates, and only those shear jammed (including fragile) with $\phi \geq \phi_F$ = 0.57 has f_{nr} reach or exceeds 0.855 at steady state (γ = 1.6 ~ 2.0). These findings suggest that the special value of $f_{nr,\,jam}$ = 0.855 can serve as a criterion to separate unjammed and (shear) jammed states, regardless of the initial phase of the specimen. A similar threshold $f_{nr,\,jam} \approx 0.83$ is reported for 2D granular disk assemblies in pure shear experiments.[14] However, this does not imply that $f_{nr,\,jam}$ is a universal value across various system configurations. Instead, it is contingent on system parameters such as grain size distribution, contact model, interparticle friction coefficients, preparation protocols, system sizes, etc.

The steady-state values of non-rattler fraction $f_{nr,st}$ are plotted in Fig. 4(b) with the error bar indicating the fluctuation of f_{nr} in the range of γ = 1.6 ~ 2.0. It is observed that f_{nr} fluctuates significantly for very loose specimens with ϕ = 0.45 ~ 0.50, a sign of highly unstable fabric structure despite the specimen has undergone a long time of shearing. In contrast, the error bar of $f_{nr,st}$ reduces considerably for medium loose specimens with ϕ = 0.51 ~ 0.56 < ϕ_F, meaning that a relatively stable fabric structure is developed at steady state for unjammed medium loose specimens. Specimens with $\phi \geq \phi_F$ = 0.57 are all jammed during shear and have negligible error bar associated with their $f_{nr,st}$ data. Similar to Fig. 3(a), the evolution trend diverges at ϕ_F, and $f_{nr,st}$ vanishes as ϕ decreases following a power law pattern when $\phi \geq \phi_F$ = 0.57. An equation similar to Eq. (13) with $f_{nr,jam}$ = 0.855 is proposed:

$$f_{nr,st} - f_{nr,jam} = a_2 \left(\phi - \phi_c\right)^{b_2} \tag{15}$$

and the best-fit parameters yielding R^2 = 0.9927 are a_2 = 0.3133 and b_2 = 0.3215 and ϕ_c = 0.5700, as shown in the subplot in Fig. 4(b). The minimal disparity observed in the calibrated jamming-ϕ values between Fig. 3(a) and Fig. 4(b) underscores the consistency and robustness of the results, as well as the reliability of the obtained jamming threshold ϕ_F.

3.3 Classical jamming phase diagram

The JPD in the τ-ϕ plane is presented in Fig. 5(a) by taking the steady state shear stress τ as

the yield stress for each ϕ. The value of τ at jamming-unjamming transition gradually increases with ϕ as expected. The two previously identified special values for ϕ are marked, namely ϕ_F = 0.57 where shear jamming occurs and ϕ_J = 0.638 where isotropic jamming occurs.

It is worth noting that the original definition of fragile[13] – "The inability to elastically support some infinitesimal loads along the incompatible directions" – is a highly conceptual one. Quantitative measures must be adopted to practically observe fragility and distinguish it from shear jamming in experiments. In some studies[9], a granular packing is defined as fragile or shear jammed when the strong contact network percolates in only one direction or in all directions, respectively. This visual-based criterion can be ambiguous depending on how one perceives percolation. In other studies[14], the fragile and shear jammed states are defined by whether p falls below or above p_{noise}, respectively, during the first loading reversal. This can introduce arbitrariness as well, as medium-loose granular packings may still resist shear during the first few cycles of stress reversal but have p drops to 0 in the subsequent cycles under undrained (i.e., constant ϕ) condition. This is a well-studied phenomenon called "cyclic liquefaction" in the soil mechanics literatures.[32, 33, 73, 74] Therefore, the concept of fragile and its boundary with respect to the shear jammed state in JPD remains somewhat ambiguous and worth further investigation.

On the other hand, several studies[9, 14, 75] suggested that there is a curved boundary between the jammed and shear jammed phases in τ-ϕ plane at $\phi > \phi_J$ regime. This may be inherited from the unjammed-jammed boundary in the original JPD for frictionless particles,[1, 35] and implies that an initially jammed specimen can transit to shear jammed state when sheared under constant ϕ. It is however not at all clear what macroscopic signals correspond to this transition. To avoid ambiguity, a straight vertical line at ϕ_J is regarded as the boundary between the jammed and the shear jammed phases in Fig. 5, since specimens with $\phi_F \leq \phi < \phi_J$ in our simulation are initially unjammed but can be jammed under the introduction of shear stress, and the packing with $\phi \geq \phi_J$ is isotropically jammed before shearing. To summarize, in τ-ϕ plane (Fig. 5(a)), we define: (1) specimens falling within the

range of $\phi_F \leq \phi < \phi_J$ and $\tau < \tau_{yield}$ as belonging to the fragile or shear jammed state (F/SJ); (2) region of $\phi \geq \phi_J$ and $\tau < \tau_{yield}$ as jammed (J); (3) the rest as unjammed (UJ).

The JPD in the p-ϕ plane is presented in Fig. 5(b). It exhibits a similar boundary between the UJ and the F/SJ phases as the one identified in ref. 14. Here we have further enriched the diagram by considering the $\phi > \phi_J$ regime and adding the conceptual DSL discussed in Fig. 3(b) after axes transformation. The region beyond DSL cannot be accessed unless processes such as particle breakage starting to alter the grain size distribution and the grain morphology of the specimen.[76-78] Comparing Fig. 3(b) with Fig. 5(b), it is instructive to see that the well-established CSL in soil mechanics literature is essentially the same as UJ to F/SJ phase boundary in JPD. This equivalence permits the cross comparison between existing studies in both communities, which may inspire new directions of granular mechanics/physics research. In what follows, we inspect the fabric states of all tested specimens in an attempt to identify the microstructural patterns that control the phase transition of granular materials.

4 Jamming phase diagram in fabric space

4.1 Fabric evolution

The non-ratter, total-, and strong- contact coordination numbers (i.e., Z_{nr}, Z_t and Z_s) and fabric anisotropies (i.e., F_{nr}, F_t and F_s) in the simulations are presented in Fig. 6. The left figures show the evolution of Z's with respect to γ. It is observed that the Z's of specimens with $\phi = 0.45 \sim 0.63$ (initially unjammed) gradually increase to steady state, while the Z's of initially jammed sample ($\phi = 0.64$) evolve to a steady state lower than the initial value. Just as in the preceding section where we established the jamming threshold as $p_{noise} = 3$ kPa and $f_{nr} = 0.855$, we now adopt the steady state Z value of specimens with $\phi = 0.57$ as the jamming threshold (Z_{jam}) to distinguish between unjammed and jammed states.

The right figures show the evolution of F's with respect to γ. Since the specimens are initially isotropic, all F's start at zero. The F_{nr} exhibits significant oscillations for unjammed specimens during initial shearing, which is expected as only a few contacts present at that stage and most particles are rattlers. The F_{nr} eventually stabilizes and reaches a steady state,

with value being lower for denser specimens. The steady-state F_t decreases slightly with ϕ when specimen is jammed ($\phi \geq \phi_F$) and increases moderately with ϕ when specimen is unjammed ($\phi < \phi_F$), while the steady-state F_s is always higher for larger ϕ specimens, consistent with our previous findings.[32, 33] Note that the specimens of $\phi < 0.57$ have never been jammed at any stage of shearing but still has finite F_{nr} and F_t. This reveals an important but often neglected property of frictional granular materials: even loose quasi-static granular flow exhibiting $p \approx 0$ can develop distinct fabric anisotropy amid the dynamic creation and destruction of contact network after sufficient shearing. The fabric structure of unjammed granular systems has only gained some attention recently. In soil mechanics research, non-trivial fabric anisotropy in liquefied ($p \approx 0$) granular soils during continuous shearing has been recently observed.[32, 33, 79] Studies on concentrated granular suspensions have also reported the development of anisotropic microstructure when shear is applied.[80] Augmented by our present observation that all specimens (UJ, F/SJ, and J) demonstrate finite F_{nr} and F_t after undergoing adequate shearing, it is justifiable to conclude that a steady-state granular flow consistently maintains microstructural anisotropy. This point will be further elaborated in the next section.

4.2 Fabric path and critical fabric surface

Fig. 7 presents the evolution path of fabric data throughout shearing ($\gamma = 0.0 \sim 2.0$) in the left plots and the steady-state fabric data (after the sample reaching steady-state shearing, $\gamma = 1.6 \sim 2.0$) in the right plots on the F-Z plane. It is observed from Figs. 7(a)(c)(e) that the fabric paths of initially unjammed specimens ($\phi < 0.63$) always start at their minimum values (2 for Z_{nr}, 0 for Z_t and Z_s and F_t and F_s). The initial F_{nr} is quite scattered since the specimens near the extreme of $f_{nr} \rightarrow 0$ do not have a stable non-rattler contact network yet, and the occasional percolation of force chains along certain direction is registered as high initial F_{nr} values. Shearing drives their fabric paths towards higher Z value and eventually ceases evolving around the steady state (Z_{st}, F_{st}) identified in Figs. 6. For the initially jammed specimen ($\phi = 0.64$), its fabric paths start at a large coordination number ($Z_{nr} = 6.79 > Z_{nr,\,jam}$, $Z_t = 6.72 > Z_{t,\,jam}$, $Z_s = 2.78 > Z_{s,\,jam}$) with negligible anisotropy due to the initial isotropic

compression. During the course of shear, the values of its F's ascend to their peak and subsequently drops to reach the CFS defined later, a trend concurrent with the reduction followed by an increase in the values of Z.

Figs. 7(b)(d)(f) presents only the steady-state fabric data ($\gamma = 1.6 \sim 2.0$). All three types of fabric measures clearly exhibit a steady-state fabric envelope on the F-Z plane. They are referred to as the Critical Fabric Surface (CFS) hereafter to be consistent with Fig. 1 and our previous works.[30, 32, 33] Different types of equations are tried to capture the steady state fabric data. The power-law function (Eq. (16)) and the Gunary function[81] (Eq. (17)) are adopted to best fit the CFS of the non-rattler, total-, and strong- contact fabrics respectively for their simplicity as well as the relatively high R^2 values achieved.

$$f(x) = a_3 x^{b_3} \tag{16}$$

$$f(x) = x \Big/ \left(c_1 + c_2\sqrt{x} + c_3 x\right) \tag{17}$$

The parameters for the best-fit CFS expressions are $a_3 = 12.18$ and $b_3 = -0.8557$ for non-rattler CFS with $R^2 = 0.9765$; $c_1 = 0.7674$, $c_2 = -0.8659$ and $c_3 = 0.584$ for total contact CFS with $R^2 = 0.9755$; $a_3 = 1.845$ and $b_3 = 0.6976$ for strong contact CFS with $R^2 = 0.9960$.

Fig. 7(d) indicates that the steady-state fabric anisotropy of total contact network $F_{t,\,st}$ diminishes as Z_t approach to zero. It is therefore conceivable that in extremely loose packings (e.g., granular gas), particles will barely touch each other throughout quasi-static shearing, and the contact based CFS will no longer be descriptive of the material's fabric. To investigate this, an additional set of tests are conducted on extremely loose samples ($\phi < 0.45$) and observed that the fabric information was no longer reflected in CFS when $\phi = 0.40$. For the non-rattler CFS in Fig. 7(b), the data of $\phi = 0.40$ is highly scattered with $F_{nr,\,st}$ is in the range of $4 \sim 12$ and $Z_{nr,\,st}$ lies near the minimum value 2. In this case, only a few local non-rattler fabric clusters exist, and the calculated fabric tensor will be no longer representative for the whole packing. For the total- and the strong- contact CFS in Figs. 9(d) and (f), the data of $\phi = 0.40$ locates around the origin, meaning the fabric structure is hardly detectable even if external energy is continuously supplied by shearing. From this purely geometrical

standpoint, a ϕ_G that exists in the range of $0.40 \leq \phi < 0.45$ may be defined to separate the granular gas (G) and the granular liquid (UJ) regimes, in analogues to $\phi_F = 0.57$ and $\phi_J = 0.638$ that respectively distinguishes the UJ to F/SJ and F/SJ to J transitions in the JPD in Fig. 5. Our earlier speculation in Section 4.1 can now be put in stricter terms: steady-state granular flow with $\phi > \phi_G$ is always microstructurally anisotropic with non-zero Z's, regardless of whether it is initially jammed or unjammed.

It is worth noting that the present DEM simulations are drastically different from authors' previous studies[32, 33] in terms of the shear mode (simple shear vs. triaxial shear), contact model (Hertz-Mindlin vs. linear), grain size distribution (bi-disperse vs. polydisperse), and the control mechanism (athermal quasi-static shear vs. boundary-only control), yet the shapes of the obtained CFS's are surprisingly similar. Indeed, the total- and strong- contact CFS in Figs. 7(d)(f) and previous works[32, 33] are all satisfactorily described by Eqs. (16) and (17) with slightly different parameters, respectively. Therefore, the unifying power of CFS lies in that it describes the steady-state fabric of all specimens regardless of their phase states, and is also robust and insensitive to the shear mode. Different portions of CFS host the steady-state fabric data of samples with different packing fractions denoted by different colors in Figs. 7(b)(d)(f). This hints that there exists a direct relation between the UJ – F/SJ phase boundary on the JPD and the CFS in the *F*-*Z* plane, and possibly a one-to-one mapping between different phases and the regions surrounding CFS. We shall explore this in the next section.

4.3 Jamming phase diagram in fabric space

By inspecting the fabric paths in Fig. 7, we map the granular phases defined in Fig. 5 to the fabric *F*-*Z* plane for the non-rattler and the total contact networks in Fig. 8. The strong-contact plot is omitted since its shape is qualitatively similar to that of the total-contact plot. It features the following regions:

(1) The entire CFS and its immediate vicinity forms a narrow band collecting the steady-state fabric data, thus it is denoted as the "Flow steady" region.

(2) Samples with Z smaller than Z_{jam} and F above CFS are macroscopically identified as unjammed (i.e., $p \approx 0$). Their microstructures are still evolving with respect to γ (see Figs.

6(b) and (d), γ = 0~0.8) and have not arrived at the CFS yet. Correspondingly, this region is denoted as "Flow transient" marked by the light gray color in Fig. 8. In this stage, the initial fabric induced by the preparation protocol is still being "remembered" by the specimen, and the term "transient" here refers to the microstructure being in transition to a new steady-state configuration driven by quasi-static shear γ. This term therefore should not be confused with the transient processes discussed in dynamic settings where time is the driving variable. The fabric paths of all UJ specimens ($\phi < \phi_F$) evolves within the Flow transient region and end at the Flow steady portion left to the Z_{jam} line.

(3) For F/SJ specimens ($\phi_F \leq \phi < \phi_J$), their fabric path will travel through the "flow transient" region, pass the Z_{jam} line, enter the "F/SJ" region marked by the red and green color, and finally reach the joint area of the "Flow steady" and the "F/SJ" regions. Although the fragile and shear jammed states are not distinguished in the present study, we hypothesize that specimens jammed at low Z values are more likely to be fragile and those reach relatively high Z are shear jammed. This is supported by the original definition of fragile[13] that force chain inside the granular packing is percolated along one direction but is disconnected along the other direction, which corresponds to high F but low Z values. The exact boundary between the F and the SJ phases still needs to be systematically investigated in the future.

(4) The possible fabric states of jammed specimens ($\phi \geq \phi_J$) are marked by the dark gray zone based on the data in Fig. 7 and complemented by Fig. 1(a). The fabric states of jammed specimens eventually reach the "Flow steady" region at very high Z values as γ accumulates. Some overlap between the jammed and the SJ phases appear. This suggests that the same fabric state (Z, F) can be reached by specimens with different ϕ and phase states. Such overlapping could be attributed to the inability of the second-order fabric tensor E_{ij} in representing the full fabric information of a granular specimen. Comparing the higher-order fabric components or directly the $\rho(\mathbf{n})$ in the joint SJ-J regions may reveal the differences between the fabric structures of the two specimens.[33]

There are also some blank zones in Fig. 8 where no fabric data from the present

simulation campaign are found. These zones are labeled as 'A', 'B' and 'C'. Our previous study[32, 33] and new simulations not reported here suggest that fabric states can indeed exist in region 'B' by stress reversals. For example, by performing unloading on a specimen in the 'F/SJ' or 'Flow steady' regions, the coordination number remains similar, but fabric anisotropy drops, and the fabric path moves downward to 'B'. When cyclic stress reversal is applied on initially jammed specimens, Z will gradually decrease and the phase state moves leftward to region B.[33] We also found that preparing specimens at $\mu > 0$ permits an initially jammed state at a relatively loose packing $\phi_J < \phi_{RCP}$.[32] This puts the specimen's initial fabric state in region B directly, and shear drives the fabric path across region B and reaches CFS (Fig. 1(a)).

Region 'A' represents the unjammed state since $Z < Z_{jam}$. However, we didn't find any data exists in 'A' based on our present and previous simulations. The fabric state for jammed specimens jumps from $Z > Z_{jam}$ to the origin of coordinates upon unjamming (or liquefaction) irrespective of whether it is induced by monotonic or cyclic shearing, and the fabric state of liquefied specimens jumps from 'Flow transient' to the origin of coordinates upon loading reversals.[33] Further investigations are needed to determine whether region 'A' is truly inaccessible for quasi-statically sheared granular materials.

In all of our simulations, region 'C' characterized by high F values has never been reached and is deemed to be inaccessible. For a fixed coordination number, large F means all contacts are aligned along one direction but not supported laterally. This could result in the buckling of the force chain and thus unstable contact network, providing an explanation for the lack of fabric states in "C" for granular materials at the quasi-static limit. The accessibility of fabric states due to local geometrical constraints has been also discussed in analytical settings[34].

Identifying the fabric characteristics underlying different phases creates the possibility to determine the state of granular materials solely through kinematical measures such as optical methods or X-ray tomography without the need to ascertain the stress state of the specimen. In industrial applications, gaining access to the stress state within a granular flow undergoing

553 complex boundary conditions is usually inpractical.[82] Utilizing geometry-based methods to
554 identify phase states can provide valuable insights into the efficiency of granular system and
555 serve as a guide for future optimization efforts. Furthermore, the fabric-based phase diagram
556 (Fig. 8) can furnish insights into whether a granular packing is at a transient state or has
557 attained a final steady state, which serves as a valuable feature in geoscience studies in
558 determining the shear history of granular materials in certain regions (e.g., fault gauge).[83, 84]

559 5. Fabric – f_{nr} relation

560 Fig.9 investigates the relation between contact fabrics and the non-rattler fraction f_{nr}. It
561 is observed from Fig. 9(a) that all the $Z_{nr} - f_{nr}$ data fall within a narrow band. Similar
562 observation has been reported from pure shear photoelastic experiments.[9, 85] This suggests
563 that Z_{nr} and f_{nr} maintain a robust relationship that presents in both 2D and 3D granular
564 specimens. The total coordination number Z_t appears to correlate even better with f_{nr} as
565 shown in Fig. 9(c). All data effectively collapse into a curve, regardless of whether the
566 sample being UJ, F/SJ, or J throughout the shearing process. By plotting the $Z - f_{nr}$ data of
567 only unjammed specimens in the subplots of Figs. 9(a)(c), we confirm that the sample
568 remains unjammed when $f_{nr} < 0.855$ but will enter F/SJ or J phases once f_{nr} exceeds this
569 value.

570 Figs. 9(b)(d) show that the normalized fabric anisotropy $\overline{F}_{nr} = F_{nr} / Z_{nr}$ and $\overline{F}_t = F_t / Z_t$
571 decrease as f_{nr} increases, confirming that denser and more jammed granular packings develop
572 less normalized fabric anisotropy.[21, 32] Similar to the $Z - f_{nr}$ plots, all the $\overline{F}_{nr} - f_{nr}$ and $\overline{F}_t - f_{nr}$
573 data collapse into a narrow band. The correlation is improved for the steady-state data as
574 shown in the subplots of Figs. 9(b)(d). It shows that the steady-state $\overline{F}_{nr} - f_{nr}$ and $\overline{F}_t - f_{nr}$
575 lines are essentially identical. Furthermore, in Fig. 9(e), the correlation between the steady-
576 state normalized fabric anisotropy $\overline{F}_{nr,\,st}$ and $\overline{F}_{t,\,st}$ data is striking similar, clustering around
577 the around the 1:1 line with $R^2 = 0.9985$, although $\overline{F}_{t,\,st}$ contains extra fabric data about the
578 rattlers. This suggests that the contact network of rattlers in the steady state is not random or

isotropic; instead, it aligns with the same major direction or anisotropy as that of the non-rattler contact network. To demonstrate this, Fig.10 presents the polar histogram of non-rattler- and rattler- contact normals' probability distribution density in y-z plane of the specimen with $\phi = 0.57$ at $\gamma = 0$, 0.2, 1.0 and 2.0, respectively. In Fig. 10, the radius of each bin represents the (number of contact normals in the bin) / (number of all contact normals) / (width of each bin, i.e., 20° = 0.3491 rad). Fig. 10 (a)-(d) shows that the non-rattler contact network initially does not exist, then begins to exhibit some degree of anisotropy at $\gamma = 0.2$, followed by a slight decrease as it stabilizes into a steady state. This pattern is consistent with the observations in Fig. 6(b). On the other hand, Fig. 10 (e)-(h) shows that a random rattler-contact network exists prior to shearing. As shearing proceeds, a distinct level of anisotropy emerges within the rattler contact distribution, and this anisotropy aligns with a direction akin to that observed in the non-rattler contact network.

6. Concluding remarks

This study investigates the fabric structure of frictional granular materials near jamming transition though a series of constant-ϕ quasi-static simple shear DEM tests. The fabric structure characterized by three different contact networks is analyzed in terms of coordination number (Z), fabric anisotropy (F), and non-rattler fraction (f_{nr}). A unifying Critical Fabric Surface (CFS) for both unjammed (UJ) and jammed (F/SJ, J) granular packings is found in F-Z plane. In addition, a novel jamming phase diagram in the fabric F-Z plane is proposed, and its potential applications are discussed. The main conclusions of this study are summarized below:

(1) The boundary between the unjammed and jammed phases in the JPD within the p-ϕ plane is equivalent to the critical state line frequently discussed in soil mechanics literature within the e-p plane. In addition, the p-ϕ JPD should incorporate a densest state line at higher ϕ values. Beyond this line, states become inaccessible unless certain processes, such as grain crushing, begin to modify the grain size distribution and the grain morphology.

(2) By plotting the fabric paths of all samples on the F-Z plane, we identified a unique CFS

that attracts the fabric state (including the non-rattler, total, and strong contact networks) of granular assemblies upon shearing. This observation underscores that a steady-state granular flow with $\phi > \phi_G$ consistently exhibits microstructural anisotropy, irrespective of whether it is jammed or unjammed.

(3) We proposed a conceptual JPD in the fabric *F-Z* space. The fabric JPD provides a geometrical metric for assessing the phase state of granular materials, complementing the conventional JPD in which information regarding the stress state of the assembly is necessary. This approach offers a fresh perspective for understanding the jamming phenomenon, potentially serving as a source of inspiration for researchers in both granular physics and geomechanics.

(4) Our simulation shows a one-to-one relation between the non-rattler fraction f_{nr} and the coordination numbers Z_t *and* Z_{nr} for all samples throughout shearing. The rattler particles do not exhibit an isotropic distribution during shearing; instead, they tend to align along the direction where the total fabric anisotropy emerges. A threshold non-rattler fraction $f_{nr,jam}$ = 0.855 that separates jammed and unjammed packings is identified. This value is close to 0.83 that was identified in prior 2D photoelastic experiments.[9]

One limitation of the present study is that the fragile and shear jammed states are not distinguished due to the absence of stress reversal in the loading program and also the lack of a quantitative definition of fragile. The JPDs constructed in this study therefore do not separate the fragile and the shear jammed phases in both the conventional τ-ϕ space and the fabric *F-Z* space. The clarification between different criterions for the determination of fragile and precise determination of its region in the phase diagram worth a systematic study, which is one of the primary goals in our follow up studies. An additional limitation is the omission of highly stochastic characteristics in the unjamming-jamming transition within the current simulation, which is known to be significantly influenced by finite size effects. The statistical uncertainties in determining the jamming/unjamming boundary in the JPD requires further refinement to clearly elucidate this aspect in future investigations.

Author contributions

Yuxuan Wen conducted the simulation, performed the analysis, and drafted the manuscript. Yida Zhang initiated the conceptualization, secured funding, provided supervision, and revised the manuscript.

Conflicts of interest

There are no conflicts of interest to declare

Acknowledgements

This research was supported by the U.S. National Science Foundation (NSF) under NSF CMMI Award No. 2237332 and the Predictive Science Academic Alliance Program (PSAAP) under Award No. DE-NA0003962. The authors would also like to acknowledge Dr. Yiqiu Zhao (currently at Hong Kong University of Science and Technology) for the enormous help and constructive discussions throughout this study.

References

1. J. Liu and S. R. Nagel, *Nature*, 1998, **396**, 21-22.
2. R. P. Behringer, *Comptes Rendus Physique*, 2015, **16**, 10-25.
3. R. P. Behringer and B. Chakraborty, *Reports on Progress in Physics*, 2019, **82**, 012601.
4. C. S. O'Hern, S. A. Langer, A. J. Liu and S. R. Nagel, *Physical Review Letters*, 2002, **88**, 075507.
5. C. S. O'Hern, L. E. Silbert, A. J. Liu and S. R. Nagel, *Physical Review E*, 2003, **68**, 011306.
6. T. S. Majmudar and R. P. Behringer, *Nature*, 2005, **435**, 1079-1082.
7. H. P. Zhang and H. A. Makse, *Physical Review E*, 2005, **72**, 011301.
8. L. E. Silbert, *Soft Matter*, 2010, **6**, 2918-2924.
9. D. Bi, J. Zhang, B. Chakraborty and R. P. Behringer, *Nature*, 2011, **480**, 355-358.
10. C. Song, P. Wang and H. A. Makse, *Nature*, 2008, **453**, 629-632.
11. G. Y. Onoda and E. G. Liniger, *Physical Review Letters*, 1990, **64**, 2727-2730.
12. S. Luding, *Nature Physics*, 2016, **12**, 531-532.
13. M. E. Cates, J. P. Wittmer, J. P. Bouchaud and P. Claudin, *Physical Review Letters*, 1998, **81**, 1841-1844.
14. Y. Zhao, J. Barés, H. Zheng, J. E. S. Socolar and R. P. Behringer, *Physical Review Letters*, 2019, **123**, 158001.
15. F. Radjai, M. Jean, J.-J. Moreau and S. Roux, *Physical Review Letters*, 1996, **77**, 274-277.
16. D. M. Mueth, H. M. Jaeger and S. R. Nagel, *Physical Review E*, 1998, **57**, 3164-3169.
17. C. S. O'Hern, S. A. Langer, A. J. Liu and S. R. Nagel, *Physical Review Letters*, 2001, **86**, 111-114.
18. M. Oda, *Soils and Foundations*, 1972, **12**, 45-63.
19. F. Radjai, D. E. Wolf, M. Jean and J.-J. Moreau, *Physical Review Letters*, 1998, **80**, 61-64.
20. L. Rothenburg and R. J. Bathurst, *Géotechnique*, 1989, **39**, 601-614.
21. J. Zhao and N. Guo, *Géotechnique*, 2013, **63**, 695-704.
22. I. Srivastava, L. E. Silbert, G. S. Grest and J. B. Lechman, *Physical Review Letters*, 2019, **122**, 048003.
23. I. Srivastava, L. E. Silbert, J. B. Lechman and G. S. Grest, *Soft Matter*, 2022, **18**, 735-743.
24. M. Wiebicke, E. Andò, G. Viggiani and I. Herle, *Acta Geotechnica*, 2020, **15**, 79-93.
25. W. H. Imseeh, A. M. Druckrey and K. A. Alshibli, *Granular Matter*, 2018, **20**, 24.
26. A. N. Schofield and C. P. Wroth, *Critical State Soil Mechanics*, McGraw-hill, London, 1968.
27. X. S. Li and Y. F. Dafalias, *Journal of Engineering Mechanics*, 2012, **138**, 263-275.
28. J. Zhao and Z. Gao, *Journal of Engineering Mechanics*, 2016, **142**, 04015056.
29. D. Liao and Z. Yang, *International Journal for Numerical and Analytical Methods in*

Geomechanics, 2021, **45**, 2433-2463.
30. Y. Zhang, X. Zhou and Y. Wen, *Journal of Engineering Mechanics*, 2020, **146**, 04020019.
31. M. Otsuki and H. Hayakawa, *Physical Review E*, 2020, **101**, 032905.
32. Y. Wen and Y. Zhang, *Géotechnique*, 2023, **73**, 439-454.
33. Y. Wen and Y. Zhang, *Acta Geotechnica*, 2022, **17**, 4297-4312.
34. F. Radjai, J. Y. Delenne, E. Azéma and S. Roux, *Granular Matter*, 2012, **14**, 259-264.
35. V. Trappe, V. Prasad, L. Cipelletti, P. N. Segre and D. A. Weitz, *Nature*, 2001, **411**, 772-775.
36. Z. Zhang, N. Xu, D. T. N. Chen, P. Yunker, A. M. Alsayed, K. B. Aptowicz, P. Habdas, A. J. Liu, S. R. Nagel and A. G. Yodh, *Nature*, 2009, **459**, 230-233.
37. M. P. Ciamarra, R. Pastore, M. Nicodemi and A. Coniglio, *Physical Review E*, 2011, **84**, 041308.
38. A. J. Liu and S. R. Nagel, *Annual Review of Condensed Matter Physics*, 2010, **1**, 347-369.
39. V. Šmilauer, V. Angelidakis, E. Catalano, R. Caulk, B. Chareyre, W. Chèvremont, S. Dorofeenko, J. Duriez, N. Dyck, J. Eliáš, B. Er, A. Eulitz, A. Gladky, N. Guo, C. Jakob, F. Kneib, J. Kozicki, D. Marzougui, R. Maurin, C. Modenese, G. Pekmezi, L. Scholtès, L. Sibille, J. Stránský, T. Sweijen, K. Thoeni and C. Yuan, 2021, DOI: 10.5281/zenodo.5705394.
40. S. R. Williams, C. P. Royall and G. Bryant, *Physical Review Letters*, 2008, **100**, 225502.
41. M. v. Hecke, *Journal of Physics: Condensed Matter*, 2010, **22**.
42. M. P. Ciamarra and A. Coniglio, *Physical Review Letters*, 2009, **103**, 235701.
43. J. K. Mitchell and K. Soga, *Fundamentals of soil behavior*, Wiley, New York, 3rd edn., 2005.
44. M. R. Kuhn, W. Sun and Q. Wang, *Acta Geotechnica*, 2015, **10**, 399-419.
45. X. Gu, M. Huang and J. Qian, *Granular Matter*, 2014, **16**, 91-106.
46. G. Wang and J. Wei, *Granular Matter*, 2016, **18**, 1-13.
47. C. E. Maloney and A. Lemaître, *Physical Review E*, 2006, **74**, 016118.
48. D. Fiocco, G. Foffi and S. Sastry, *Physical Review E*, 2013, **88**, 020301.
49. Z. Shojaaee, L. Brendel, J. Török and D. E. Wolf, *Physical Review E*, 2012, **86**, 011302.
50. Z. Shojaaee, J.-N. Roux, F. Chevoir and D. E. Wolf, *Physical Review E*, 2012, **86**, 011301.
51. P. Schuhmacher, F. Radjai and S. Roux, presented in part at the EPJ Web of Conferences, 2017.
52. J. Christoffersen, M. M. Mehrabadi and Nemat-Nasser, *Journal of Applied Mechanics*, 1981, **48**.
53. R. D. Mindlin and H. Deresiewicz, *Journal of Applied Mechanics*, 1953, **20**, 327-344.
54. Y. H. Xie, Z. X. Yang, D. Barreto and M. D. Jiang, *Granular Matter*, 2017, **19**, 35.
55. P. A. Cundall, in *Analytical and computational methods in engineering rock*

mechanics, ed. E. T. Brown, Allen & Unwin, London, 1987, pp. 129-163.
56. B. Chareyre and P. Villard, *Journal of Engineering Mechanics*, 2005, **131**, 689-698.
57. P. Fu and Y. F. Dafalias, *International Journal for Numerical and Analytical Methods in Geomechanics*, 2011, **35**, 1918-1948.
58. X. Li and X. S. Li, *Journal of Engineering Mechanics*, 2009, **139**, 641-656.
59. K. Kanatani, *International journal of Engineering Science*, 1984, **22**, 149-164.
60. C. Heussinger and J.-L. Barrat, *Physical Review Letters*, 2009, **102**, 218303.
61. P. Rissone, E. I. Corwin and G. Parisi, *Physical Review Letters*, 2021, **127**, 038001.
62. I. Srivastava, L. E. Silbert, G. S. Grest and J. B. Lechman, *Journal of Fluid Mechanics*, 2021, **907**, A18.
63. R. Seto, A. Singh, B. Chakraborty, M. M. Denn and J. F. Morris, *Granular Matter*, 2019, **21**, 82.
64. S. Chen, T. Bertrand, W. Jin, M. D. Shattuck and C. S. O'Hern, *Physical Review E*, 2018, **98**, 042906.
65. H. A. Vinutha and S. Sastry, *Nature Physics*, 2016, **12**, 578-583.
66. A. P. Santos, D. S. Bolintineanu, G. S. Grest, J. B. Lechman, S. J. Plimpton, I. Srivastava and L. E. Silbert, *Physical Review E*, 2020, **102**, 032903.
67. A. Donev, S. Torquato, F. H. Stillinger and R. Connelly, *Journal of Computational Physics*, 2004, **197**, 139-166.
68. A. H. Clark, J. D. Thompson, M. D. Shattuck, N. T. Ouellette and C. S. O'Hern, *Physical Review E*, 2018, **97**, 062901.
69. K. H. Roscoe, A. N. Schofield and C. P. Wroth, *Géotechnique*, 1958, **8**, 22-53.
70. M. Cubrinovski and K. Ishihara, *Soils and Foundations*, 2002, **42**, 65-78.
71. C. S. Chang, Y. Deng and Z. Yang, *Journal of Engineering Mechanics*, 2017, **143**, 04017060.
72. M. A. Maroof, A. Mahboubi, E. Vincens and A. Noorzad, *Granular Matter*, 2022, **24**, 41.
73. K. Ishihara, *Soil behaviour in earthquake geotechnics*, Clarendon Press, Oxford, 1996.
74. Z. X. Yang and K. Pan, *Soil Dynamics and Earthquake Engineering*, 2017, **92**, 68-78.
75. J. Barés, D. Wang, D. Wang, T. Bertrand, C. S. O'Hern and R. P. Behringer, *Physical Review E*, 2017, **96**, 052902.
76. G.-C. Cho, J. Dodds and J. C. Santamarina, *Journal of Geotechnical and Geoenvironmental Engineering*, 2006, **132**, 591-602.
77. A. Tengattini, A. Das and I. Einav, *Géotechnique*, 2016, **66**, 695-710.
78. Y. D. Zhang, G. Buscarnera and I. Einav, *Géotechnique*, 2016, **66**, 149-160.
79. R. Wang, P. Fu, J.-M. Zhang and Y. F. Dafalias, *Acta Geotechnica*, 2016, **11**, 1321-1337.
80. É. Guazzelli and O. Pouliquen, *Journal of Fluid Mechanics*, 2018, **852**, P1.
81. D. Gunary, *Journal of Soil Science*, 1970, **21**, 72-77.
82. A. Janda, I. Zuriguel and D. Maza, *Physical Review Letters*, 2012, **108**, 248001.
83. C. D. Rowe, J. C. Moore, F. Meneghini and A. W. McKeirnan, *Geology*, 2005, **33**,

772 937-940.
773 84. A.-M. Boullier, E.-C. Yeh, S. Boutareaud, S.-R. Song and C.-H. Tsai, *Geochemistry,*
774 *Geophysics, Geosystems*, 2009, **10**.
775 85. J. Ren, PhD PhD Dissertation, Duke University, 2013.
776

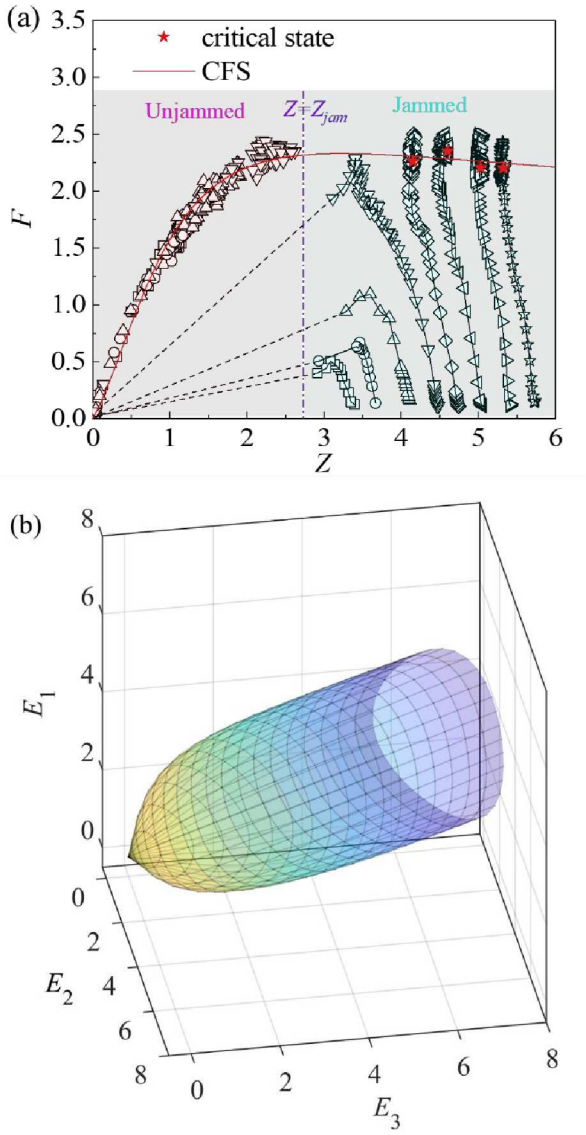

Fig. 1. (a) Critical fabric surface (CFS) and fabric evolution in *F*-*Z* plane and (b) CFS in principal fabric space, adapted from ref. 30. *Z* is coordination number; *F* characterizes fabric anisotropy; E_1, E_2 and E_3 are the major, intermediate, and minor principal values of fabric tensor E_{ij}, which can be calculated using Eqs. (7) and (9). All data were obtained from DEM simulations of constant-ϕ triaxial test on three-dimensional (3D) spherical particles. Samples were first isotropically compressed to different confining pressures, producing an initially jammed (Z's > Z_{jam}) and isotropic (F's ≈ 0) state. They are then subjected to constant-ϕ, quasi-static true triaxial shearing. Fig. 1(a) shows all fabric paths evolve to a final CFS (red line). During shearing, several specimens' fabric state (Z, F) abruptly jumped to the origin (denoted by dashed lines), experiencing sudden unjamming. With continuous application of shear strain, their fabric states evolve away from the origin following the CFS in the $Z < Z_{jam}$ range. Fig. 1(b) compiles the CFS for all true triaxial tests conducted at different Lode angles, giving a 3D CFS in the principal fabric space.

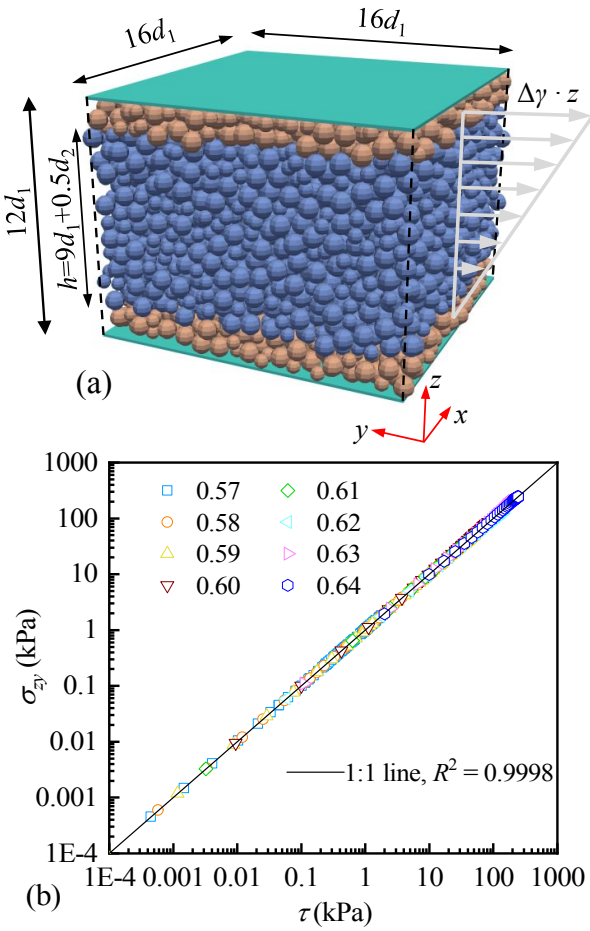

Fig. 2. Constant volume simple shear test: (a) sample during shear, where orange particles are the clumped particle-walls to impart non-trivial shear stress to the sheared particles while simultaneously preventing the escape of particles from the simulation region. Note that the simulation does not employ a wall-driven shearing algorithm. Instead, the shear strain is applied affinely to each individual particle and the two particle-walls. This is accomplished by assigning the displacement of each object directly through the utilization of the vertical coordinate and the constant shear strain increment during each timestep, followed by a subsequent relaxation stage; (b) Calibration of the effective height *h* of the specimen under shear.

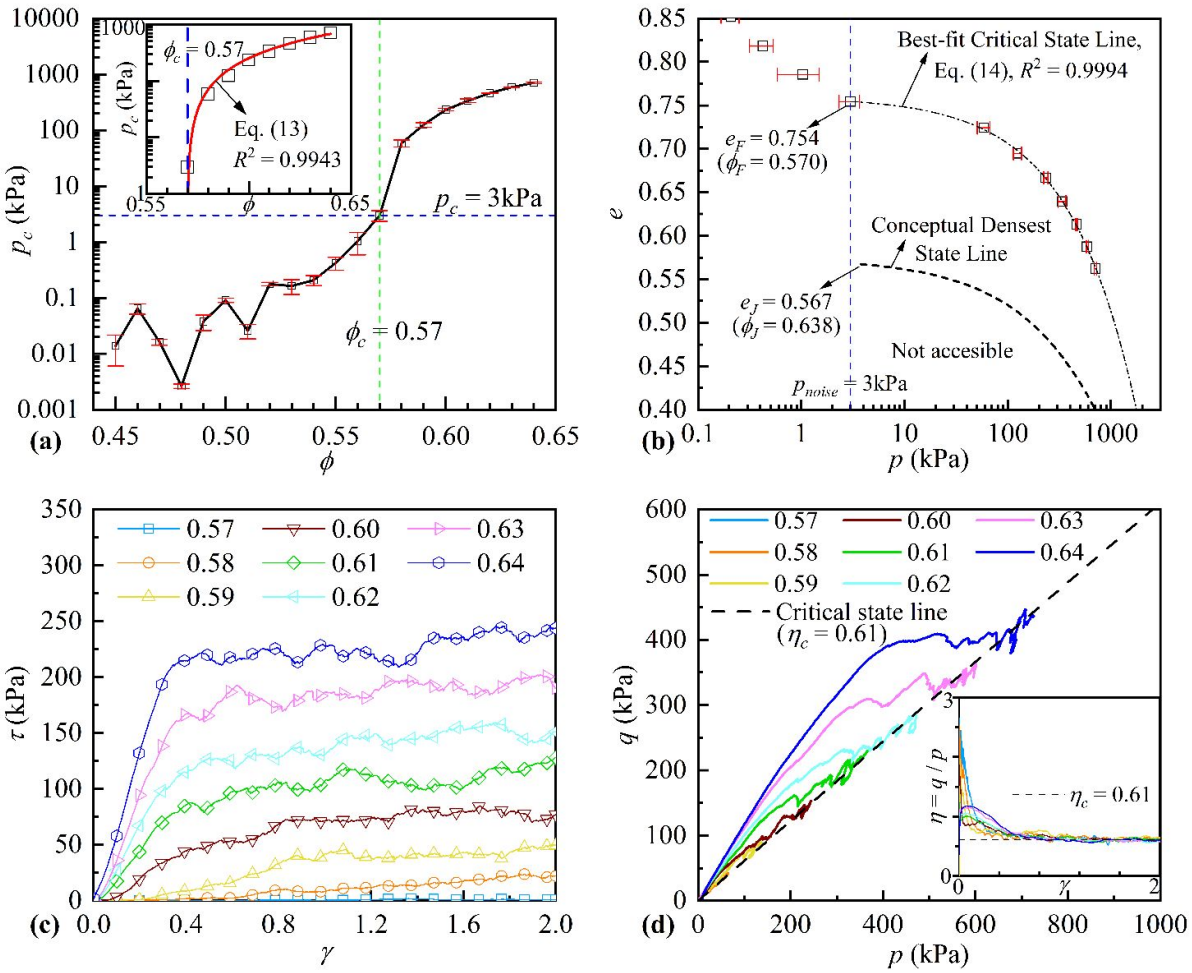

Fig. 3. Jamming thresholds in stress space: (a) determination of ϕ_F and p_{noise}; (b) determination of ϕ_J, the best-ft critical state line, and the sketched densest state line; (c) stress-strain evolution of (shear) jammed specimens; (d) stress paths and critical state stress ratio.

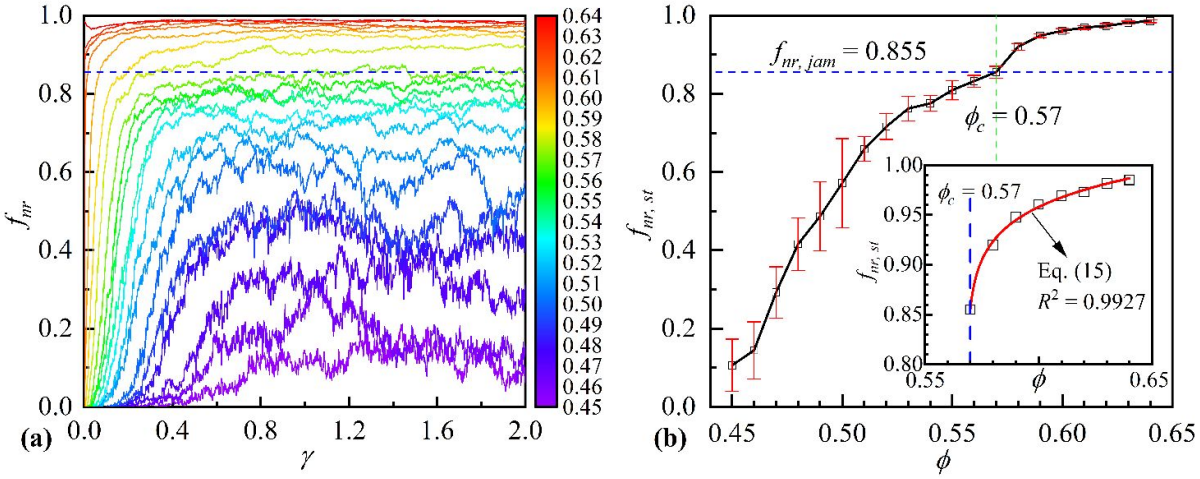

Fig. 4. Non-rattler fraction f_{nr}: (a) evolution with respect to shear strain; (b) steady-state values.

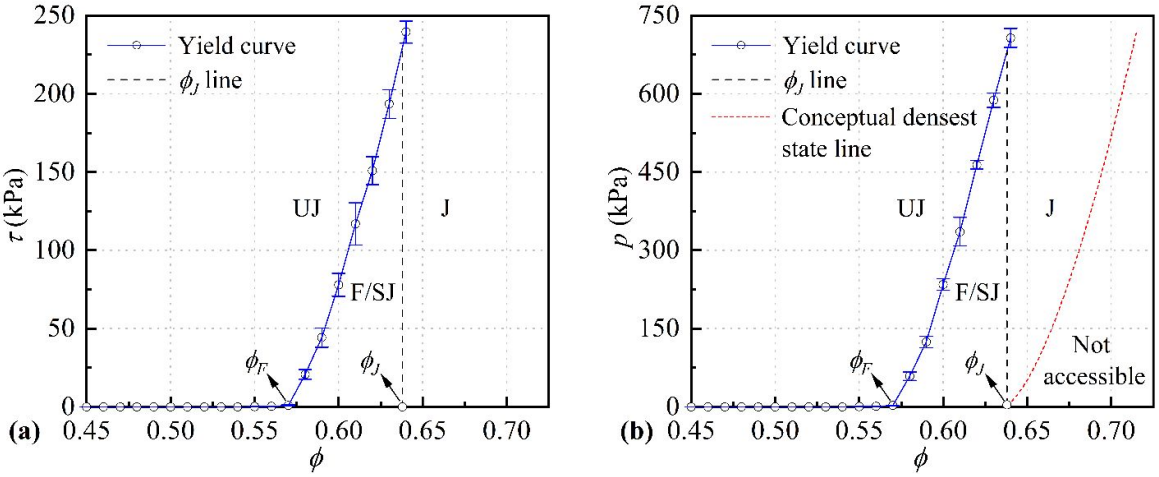

Fig. 5. Classical jamming phase diagram: (a) in τ-ϕ plane and (b) in p-ϕ plane.

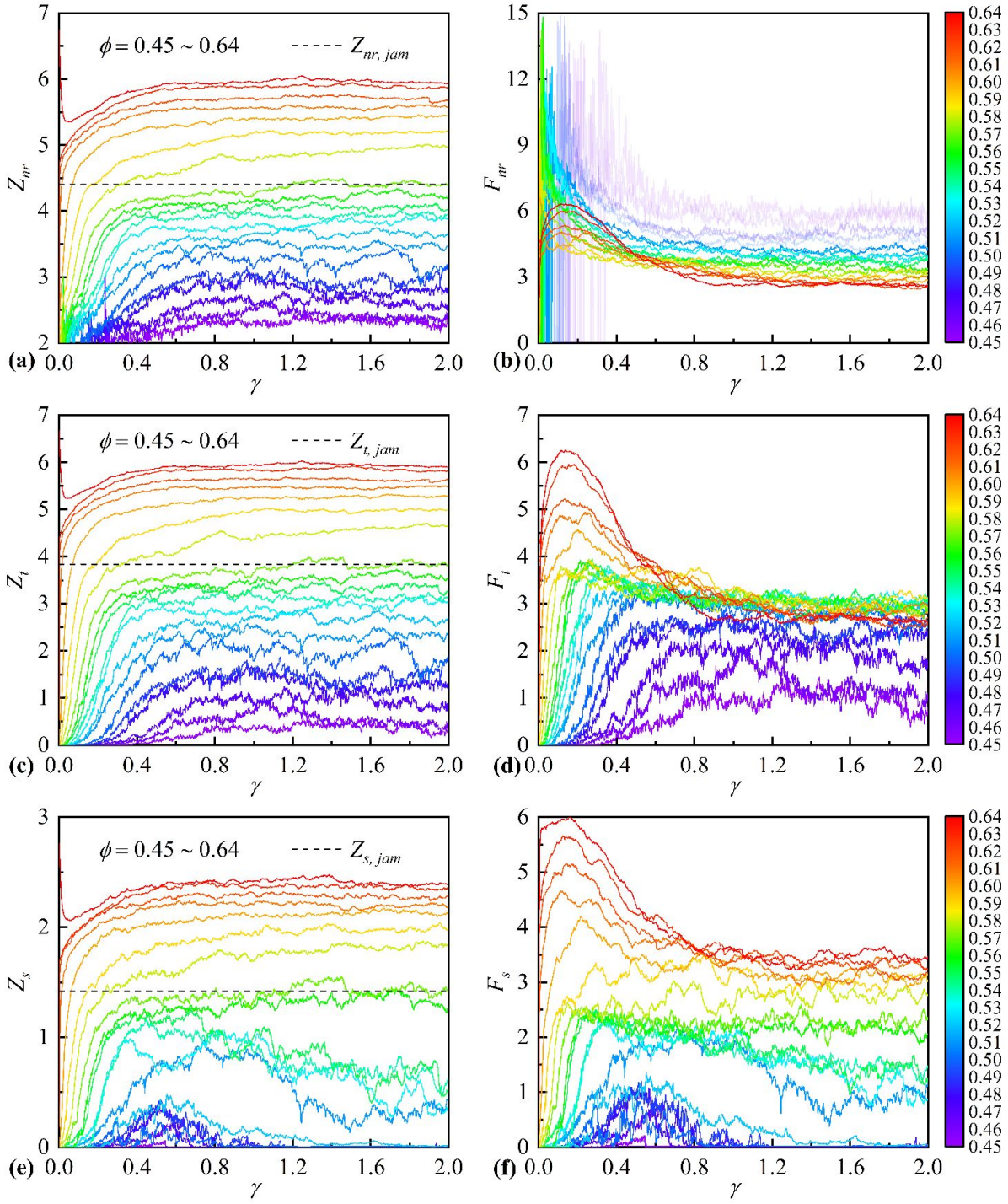

Fig. 6. Evolution of coordination numbers and fabric anisotropies: (a), (c) and (e) the evolution of Z_{nr}, Z_t and Z_s with respect to γ; (b), (d) and (f) the evolution of F_{nr}, F_t and F_s with respect to γ.

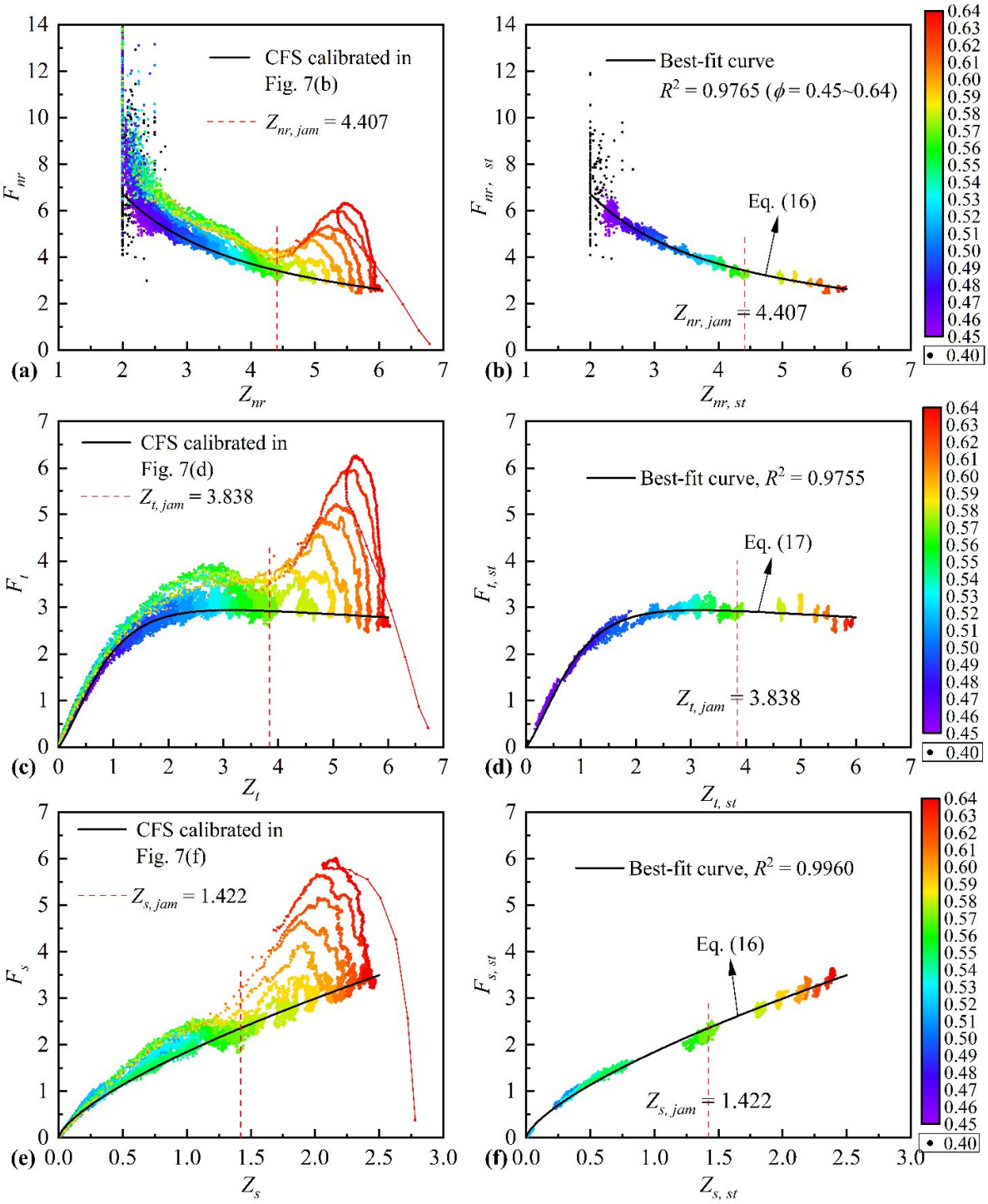

Fig. 7. Fabric paths and critical fabric surface in the *F-Z* plane: non-rattler fabric (a) paths and (b) CFS; total fabric (c) paths (d) CFS; strong fabric (e) paths and (f) CFS.

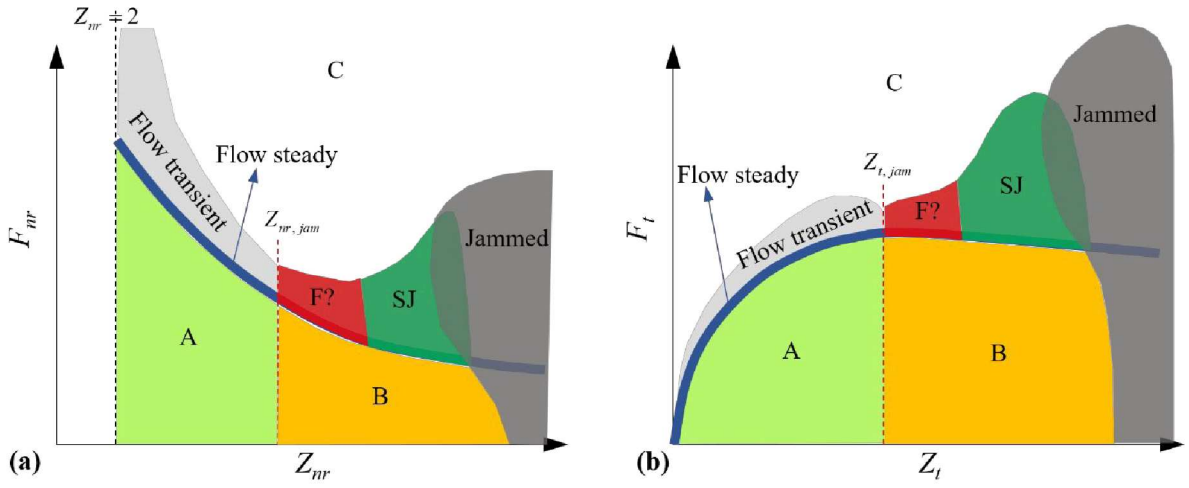

(a) **(b)**

Fig. 8. Jamming phase diagram mapped to the fabric *F-Z* space: (a) non-rattler fabric; (b) total fabric.

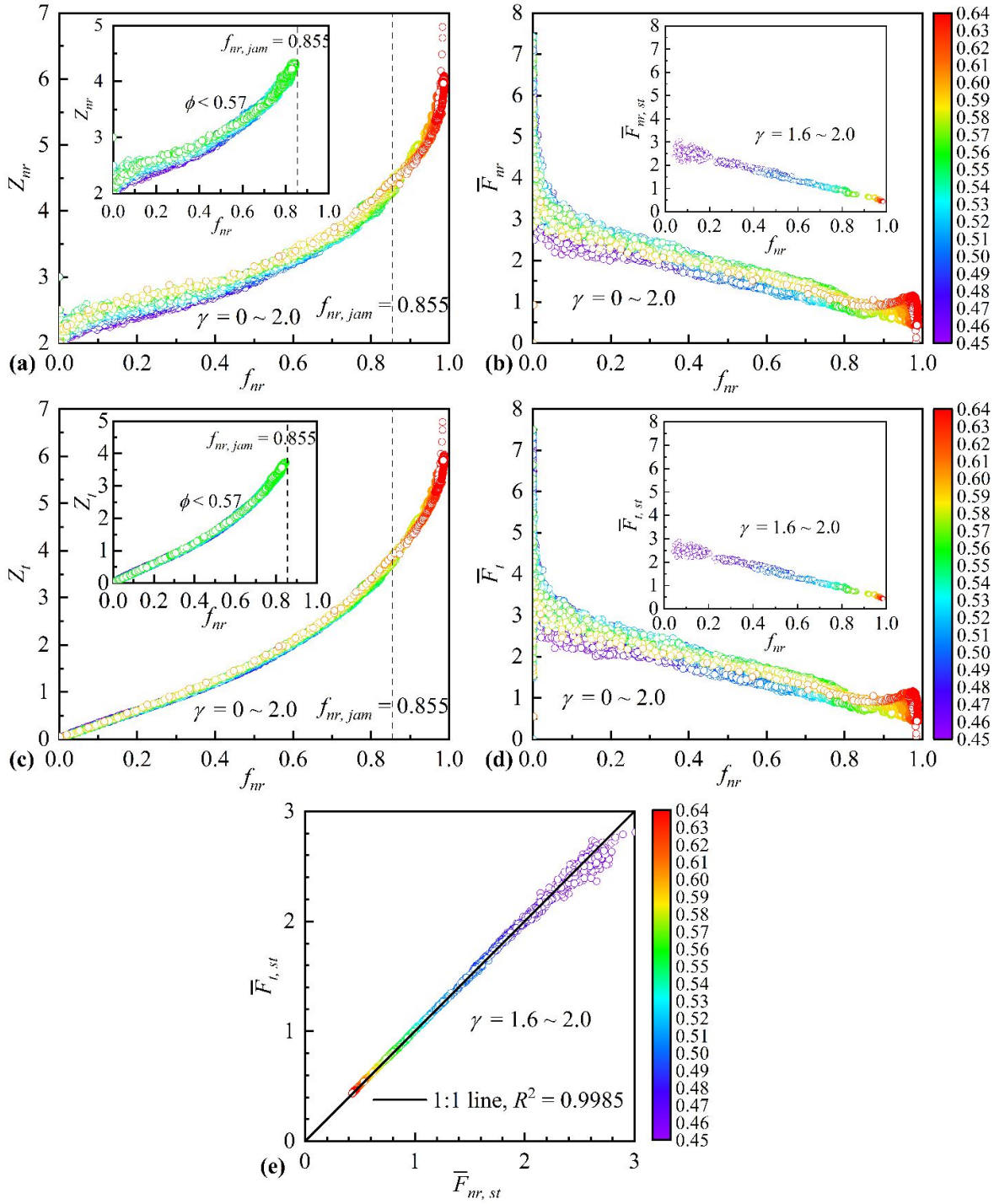

Fig. 9. Evolution of fabrics with respect to f_{nr}: (a) and (c) report the evolution of Z_{nr}, Z_t, where the subplots present the data of unjammed specimens only; (b) and (d) report the evolution of $\bar{F}_{nr}$ and $\bar{F}_t$, where the subplots show the steady state data only; (e) comparison between steady state non-rattler and total contact normalized fabric anisotropies.

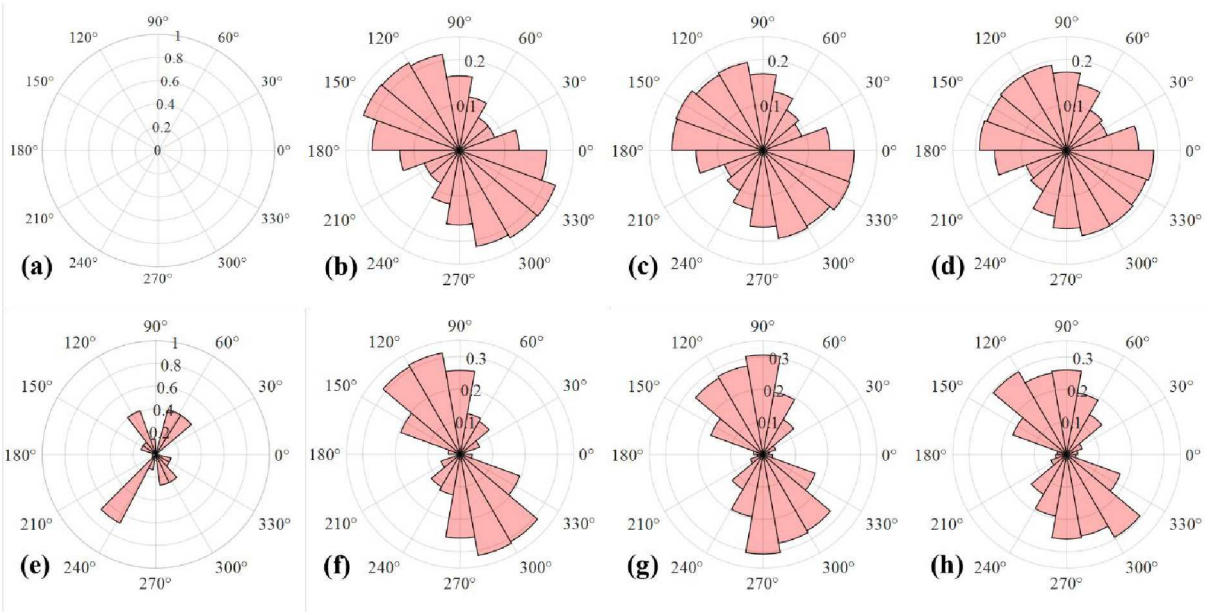

Fig. 10. Contact probability distribution density of $\phi = 0.57$ in y-z plane: (a)-(d) non-rattler contacts at $\gamma = 0$, 0.2, 1.0 and 2.0, respectively; (e)-(f) rattler contacts at $\gamma = 0$, 0.2, 1.0 and 2.0, respectively. The radius of each bin represents the (number of contact normals in the bin) / (number of all contact normals) / (width of each bin, i.e., 20° = 0.3491 rad).